Progress In Electromagnetics Research, PIER 91, 17–34, 2009

NUMERICAL MODELING AND MECHANISM ANALYSIS OF VHF WAVE PROPAGATION IN FORESTED ENVIRONMENTS USING THE EQUIVALENT SLAB MODEL

Y. Li and H. Ling

Department of Electrical and Computer Engineering
The University of Texas at Austin
Austin, TX 78712-1084, USA

Abstract—We study the radio wave propagation at VHF frequencies in a forested environment using a three-layer anisotropic slab model. The analytical solution to the slab model is implemented numerically to generate broadband data. The data are then transformed into the time domain. The various propagation mechanisms including the direct wave, the lateral wave, the multi-reflected slab waves and the multi-bounce lateral waves are investigated based on their respective times-of-flight. Our results show that the dominant propagation mechanisms are highly dependent on the effective permittivity and conductivity of the forest layer. We then utilize the numerical solution to extract the effective medium parameters of the forest based on the published measurement data of Hicks et al.. Good agreement between the fitted model and the measurement data is achieved. The extracted effective permittivity and conductivity of the forest layer show considerable anisotropy and frequency dependence.

1. INTRODUCTION

Propagation of radio waves in a forest has long been of interest since a large portion of the Earth's surface is covered by vegetation. Radio waves propagating in a forest usually experience a much higher path loss than in environments without vegetation. Therefore, understanding the propagation mechanisms through a forest is critical for communication and sensing in such environments. Researchers have proposed different models to incorporate the forest characteristics and

Corresponding author: Y. Li (yangl@mail.utexas.edu).

explain the observed forest propagation phenomena [1–12]. The most well accepted propagation model for frequencies in the HF/VHF ranges is the equivalent slab model. In this model, the forest is represented as an equivalent lossy slab layer [1, 2]. Tamir [1] pointed out that the wavelength must be sufficiently large to model the forest as a continuous medium. Since the average tree spacing in a forest is typically between 1 to 5 meters, he suggested 100MHz as the upper frequency bound for this model. Other researchers [3, 4, 6, 12] have reported that the slab characterization of the forest is accurate in the 2 MHz to 200 MHz range. Based on the slab model, Tamir [1] postulated that a lateral wave mechanism traveling along the forest-air interface is the most dominant propagation mechanism in the forest. Since the transmission loss inside the forest increases exponentially as a function of distance, he argued that the lateral wave becomes the only surviving mechanism at large distances. This lateral wave dominance has been used to explain the observed data from measurements with good success [13, 14]. In the original work of Tamir, only the forest-air interface was considered. Subsequently, the three-layer isotropic slab model for air, forest and ground was used to describe the forest environment [2–7]. By further modeling the forest as a canopy layer and a trunk layer, Li et al. [10] provided the solution to a four-layer anisotropic slab model. Since the solution to the problem is in the form of a Sommerfeld integral and not trivial to evaluate numerically, Li [12] provided detailed asymptotic analysis to extract the dominant mechanisms from the exact integral solution. Even though these asymptotic solutions are elegant and physically intuitive, their validity is limited to long distance. Due to the recent interest in networked radios at short range [15], the exact numerical integral solution is desirable.

In this paper, we implement the exact Sommerfeld integral solution to the layered forest problem. Based on the layered anisotropic solution provided by Li, the Sommerfeld integral is implemented numerically and used to generate broadband propagation data over range, height, frequency and polarization. The broadband data are then transformed to the time domain to identify the various times-of-flight. Since different propagation paths have different time delays, the propagation mechanisms are revealed in this manner. Based on the most important propagation mechanisms, a fast ray-based predictor is developed to generate an approximate solution and verify the mechanism interpretation. Finally, the Sommerfeld solution is applied to extract the effective forest parameters based on published experimental data from the measurements of Hicks et al. [16]. To ensure the validity of the slab description of the forest, the frequency

range studied in this work is limited between 25 to 100 MHz.

This paper is organized as follows. Section 2 summarizes the three-layer anisotropic slab model for the forest and the formulation of the received fields for different polarizations. The numerical implementation of the Sommerfeld integral is discussed, and results are shown. In Section 3, the resulting broadband data are transformed into the time domain, and the various propagation mechanisms are identified. A ray-optical solution is then implemented that confirms the propagation mechanisms. In Section 4, we utilize the Sommerfeld solution to extract the effective forest parameters based on Hicks' measurement data. Section 5 presents the conclusion of this study.

2. SOMMERFELD SOLUTION AND NUMERICAL IMPLEMENTATION

Figure 1 shows a three-layer anisotropic slab model of the forest. Here $\varepsilon_1 = \varepsilon_0$ and $\mu_1 = \mu_0$ denote the free space permittivity and permeability. $\overline{\overline{\varepsilon}}_2$ and $\overline{\overline{\sigma}}_2$ are the effective permittivity and conductivity tensors for the forest layer and can be combined to form a complex permittivity tensor, $\overline{\overline{\varepsilon}}_{c2}$, where:

$$\overline{\overline{\varepsilon}}_{c2} = \overline{\overline{\varepsilon}}_2 - j\frac{\overline{\overline{\sigma}}_2}{\omega} \tag{1}$$

For a uniaxial medium, it takes on the form:

$$\overline{\overline{\varepsilon}}_{c2} = \begin{pmatrix} \varepsilon_{ct} & 0 & 0 \\ 0 & \varepsilon_{ct} & 0 \\ 0 & 0 & \varepsilon_{cz} \end{pmatrix} \tag{2}$$

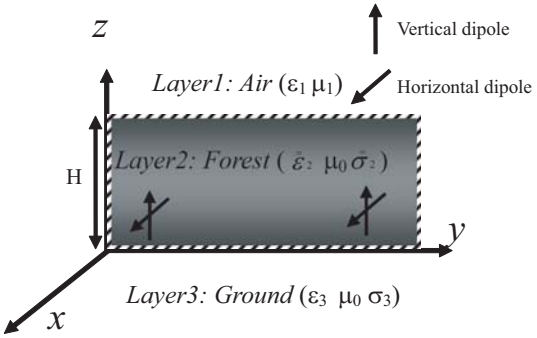

Figure 1. Three-layer anisotropic slab model of the forest.

ε_3 and σ_3 are the effective permittivity and conductivity for the ground layer, which is assumed to be isotropic. The electromagnetic propagation problem in the multi-layered slab model has been solved by Li et al. [12]. They derived the cylindrical eigenfunction expansion of the Green's dyadic for the multilayered anisotropic dielectric media. Here we specialize their solution to the three-layer problem in Fig. 1. The received field for the vertical dipole (for the $\exp(j\omega t)$ time convention) is:

$$E_{VV} = -\int_0^\infty \frac{p_z \lambda^3 J_0(\lambda r)}{4\pi\varepsilon_{cz}\omega D_2^v h_3}\left[e^{-jh_2(z_2-z_1)} - R_1^v e^{-jh_2(2H-z_2-z_1)} + R_2^v e^{-jh_2(z_2-z_1)} - R_1^v R_2^v e^{-jh_2(2H-z_2+z_1)}\right] d\lambda \tag{3}$$

The received field for the horizontal dipole is:

$$\begin{aligned} E_{HH} = -\int_0^\infty \frac{\omega\mu_0 p_x}{4\pi}\Bigg\{ & \left[\frac{\partial J_1(\lambda r)/\partial r}{h_2 D_2^H} + \frac{h_2 J_1(\lambda r)}{k_2^2 D_2^V}\right] e^{-jh_2(z_2-z_1)} \\ & - \left[\frac{R_2^H \partial J_1(\lambda r)/\partial r}{h_2 D_2^H} + \frac{R_2^V h_2 J_1(\lambda r)}{k_2^2 D_2^V}\right] e^{-jh_2(z_2+z_1)} \\ & + \left[\frac{R_1^H \partial J_1(\lambda r)/\partial r}{h_2 D_2^H} + \frac{R_1^V h_2 J_1(\lambda r)}{k_2^2 D_2^V}\right] e^{-jh_2(2H-z_2-z_1)} \\ & - \left[\frac{R_1^H R_2^H \partial J_1(\lambda r)/\partial r}{h_2 D_2^H} + \frac{R_1^V R_2^V h_2 J_1(\lambda r)}{k_2^2 D_2^V}\right] e^{-jh_2(2H-z_2+z_1)}\Bigg\} d\lambda \end{aligned} \tag{4}$$

The intermediate parameters in the above formulas are:

$$R_1^V = \frac{h_1\left[\left(\frac{\varepsilon_{cz}}{\varepsilon_{ct}}-1\right)h_{22}^2 + k_{22}^2\right] - h_{22}\left[\left(\frac{\varepsilon_{cz}}{\varepsilon_{ct}}-1\right)h_1^2 + k_1^2\right]}{h_1\left[\left(\frac{\varepsilon_{cz}}{\varepsilon_{ct}}-1\right)h_{22}^2 + k_{22}^2\right] + h_{22}\left[\left(\frac{\varepsilon_{cz}}{\varepsilon_{ct}}-1\right)h_1^2 + k_1^2\right]} \tag{5}$$

$$R_2^V = \frac{h_{22}\left[\left(\frac{\varepsilon_{cz}}{\varepsilon_{ct}}-1\right)h_3^2 + k_3^2\right] - h_3\left[\left(\frac{\varepsilon_{cz}}{\varepsilon_{ct}}-1\right)h_{22}^2 + k_{22}^2\right]}{h_{22}\left[\left(\frac{\varepsilon_{cz}}{\varepsilon_{ct}}-1\right)h_3^2 + k_3^2\right] + h_3\left[\left(\frac{\varepsilon_{cz}}{\varepsilon_{ct}}-1\right)h_{22}^2 + k_{22}^2\right]} \tag{6}$$

$$R_1^H = \frac{h_{21}-h_1}{h_{21}+h_1} \tag{7}$$

$$R_2^H = \frac{h_3-h_{21}}{h_3+h_{21}} \tag{8}$$

$$D_2^V = 1 + R_1^V R_2^V e^{-jh_{22}^2 H} \tag{9}$$

$$D_2^H = 1 + R_1^H R_2^H e^{-jh_{21}^2 H} \tag{10}$$

$$h_1 = \sqrt{k_1^2 - \lambda^2},\ h_{21} = \sqrt{k_{21}^2 - \lambda^2},\ h_{22} = \sqrt{k_{22}^2 - \lambda^2},\ h_3 = \sqrt{k_3^2 - \lambda^2} \tag{11}$$

$$k_1^2 = \omega^2\mu_0\varepsilon_1,\ k_{21}^2 = \omega^2\mu_0\varepsilon_{ct},\ k_{22}^2 = \lambda^2\left(1 - \frac{\varepsilon_{ct}}{\varepsilon_{cz}}\right) + \omega^2\mu_0\varepsilon_{ct},\ k_3^2 = \omega^2\mu_0\varepsilon_3 \tag{12}$$

In the above formulas, the subscripts denote the different layers. The symbols p_z and p_x represent the source dipole moments in the vertical and horizontal directions. Different complex permittivities in the vertical and horizontal directions in the forest layer are used to account for the anisotropic characteristics of the forest. H is the height of the forest and z_1 and z_2 are the heights of the source and the receiver, respectively. r is the radial distance between the transmitter and the receiver, and J_0 and J_1 are the zeroth and first order Bessel functions.

The above received field formulas for the vertical and horizontal dipoles are familiar Sommerfeld integrals. Due to the finite equivalent conductivity of the forest layer, the pole inside the integrand is not positioned exactly along the integration path. However, the pole is sufficiently close, especially for low-loss situations, to warrant a careful numerical integration. In order to achieve high numerical efficiency without sacrificing accuracy, the integrand is sampled densely near the pole region and sparsely away from the pole. The trapezoidal rule is applied to the integration. Another consideration is the upper limit of integration to achieve a convergent result. It is well known that the integral becomes very slowly convergent as the height difference between the transmitter and the receiver decreases [17]. In our study, the height difference in the simulation is set at a minimum of 1 m to avoid excessive computation time.

The transmission loss, which is dependent on both range and frequency, is computed as follows:

$$L_f\,(\mathrm{dB}) = 20\log_{10}\left(E_f/E_a\right) + 10\log_{10}\left[\left(\frac{\lambda}{4\pi r}\right)^2 G_T G_R\right] \tag{13}$$

where E_f represents E_{VV} or E_{HH} defined in (3) and (4), E_a represents the field that would be received at the same receiver location with the forest and the ground replaced by free space. G_T and G_R represent the gains of the transmitting and receiving antennas, respectively.

In the slab model of the forest, there are two parameters which are critical to the forest propagation mechanism study: the effective permittivity and the effective conductivity of the forest layer. These parameters could be different for different types of forest. Unfortunately, very few actual measurement results for these

parameters are available. Hagn and Parker [18] and Parker and Makarabhiromya [19] performed measurements in a large variety of vegetations and pointed out that the effective relative permittivity of a typical forest could vary from 1.01 to 1.5 and the effective conductivity could vary between 10^{-5} S/m and 10^{-3} S/m. Pounds and LaGrone [20] suggested that the effective conductivity of the forest could be as low as 10^{-11} S/m. To better understand the propagation mechanisms resulting from the slab model, we will begin by considering what we shall term a low-loss ($\varepsilon_{t2} = \varepsilon_{z2} = 1.2$, $\sigma_{t2} = \sigma_{z2} = 10^{-6}$ S/m) forest and a high-loss ($\varepsilon_{t2} = \varepsilon_{z2} = 1.2$, $\sigma_{t2} = \sigma_{z2} = 10^{-4}$ S/m) forest.

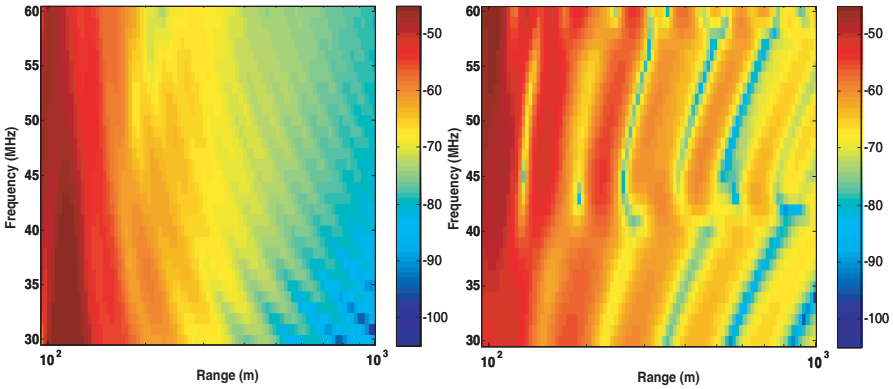

Figure 2. Transmission loss versus frequency and range, L_f, for the low-loss case with $H = 20\,\text{m}$, $z_1 = 1\,\text{m}$, $z_2 = 2\,\text{m}$, $\varepsilon_{t2} = \varepsilon_{z2} = 1.2$, $\sigma_{t2} = \sigma_{z2} = 10^{-6}\,\text{S/m}$, $\varepsilon_g = 20$, $\sigma_g = 10^{-2}\,\text{S/m}$: (a) Vertical polarization. (b) Horizontal polarization.

The transmission losses versus frequency and range for both a short vertical dipole and a short horizontal dipole in a low-loss forest are generated by computing the Sommerfeld integrals and plotted in Fig. 2. The relative permittivity and conductivity of the ground are 20 and 10^{-2} S/m, respectively. Theses values fall within the typical ground parameters in this frequency range reported in literature [3] and are consistent with our ground parameter measurements in Austin, TX using a capacitive ground probe [21]. In Fig. 2, the x axis is the distance between the transmitter and the receiver, which extends from 100 m to 1000 m. The y axis is the frequency, which ranges between 30 MHz and 60 MHz. The color scale indicates the transmission loss computed based on (13). Both the transmitter and receiver are assumed to be infinitesimal dipoles with gains of 1.5. As seen in Fig. 2, while the transmission loss decays as a function of range for both polarizations,

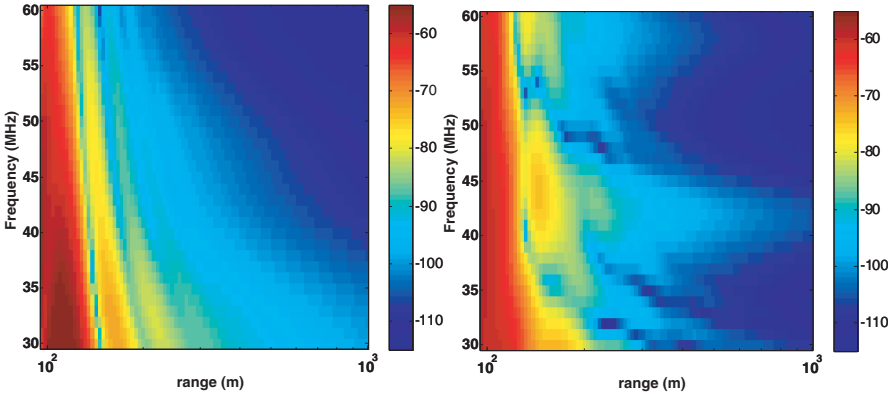

Figure 3. Transmission loss versus frequency and range, L_f, for the high-loss case with $H = 20\,\text{m}$, $z_1 = 1\,\text{m}$, $z_2 = 2\,\text{m}$, $\varepsilon_{t2} = \varepsilon_{z2} = 1.2$, $\sigma_{t2} = \sigma_{z2} = 10^{-4}\,\text{S/m}$, $\varepsilon_g = 20$, $\sigma_g = 10^{-2}\,\text{S/m}$: (a) Vertical polarization. (b) Horizontal polarization.

the strong interference patterns indicate the existence of multiple propagation mechanisms, which we will try to uncover in the next section.

Following the same procedures, we also generate the transmission loss plots for both polarizations in the high-loss forest case in Fig. 3. We observe that the fields decay much faster compared to the low-loss case for both polarizations due to the larger effective conductivity.

3. ANALYSIS OF PROPAGATION MECHANISMS IN THE FOREST

To better reveal the propagation mechanisms in the slab forest model, we convert the broadband data from the last section into time profiles via the fast Fourier transform (FFT). The frequency data, which are sampled at 1 MHz, are first windowed and then zero padded in-between data points to a sampling rate of 250 kHz. As a result, the time window is expanded to 4 µs to cover the maximum range under study. The extra periodic profiles are then removed in the final plot for clarity. The profiles for both VV and HH cases in a low-loss and a high-loss forest are shown respectively in Figs. 4 and 5. The color scale indicates the transmission loss as in the frequency plots.

From Fig. 4(a) for the low-loss VV case, two propagation mechanisms can clearly be observed. As the range increases, the propagation time difference between the two increases. The wave

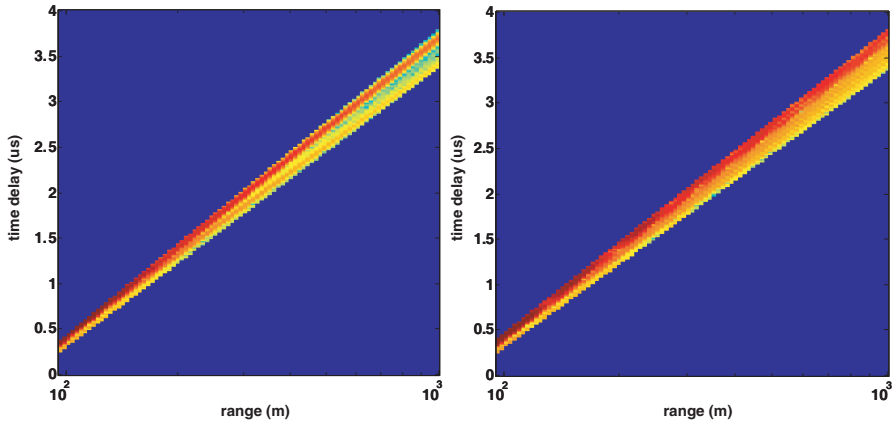

Figure 4. Transmission loss versus time delay and range for the low-loss case obtained from FFT of the broadband data in Fig. 2. (a) Vertical polarization. (b) Horizontal polarization.

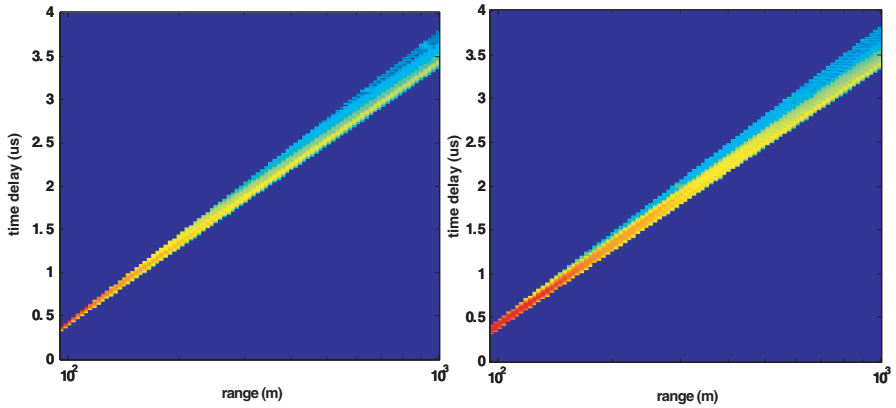

Figure 5. Transmission loss versus time delay and range for the high-loss case obtained from FFT of the broadband data in Fig. 3. (a) Vertical polarization. (b) Horizontal polarization.

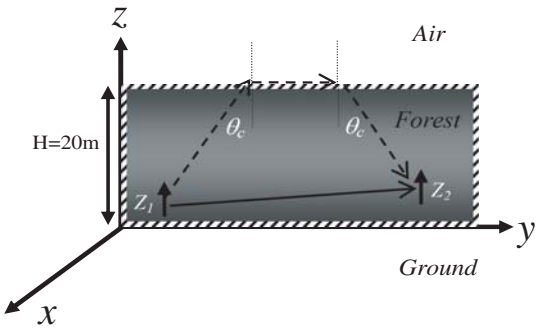

Figure 6. Direct wave and lateral wave.

arriving later is much stronger than the earlier one for a fixed distance. Based on a time-of-flight consideration, we ascertain that the earlier arriving one is the lateral wave, which is shown by the dashed path in Fig. 6. The lateral wave impinges on the forest-air boundary at the critical angle θ_c and propagates along the boundary at the air velocity, and then departs the forest-air interface at the critical angle toward the receiver. Since it spends most of the path propagating at the air velocity at long ranges, it arrives earlier compared with the wave inside the slab. The later arriving wave has time delay corresponding to the direct path which is shown as the solid line in Fig. 6. In Fig. 5(a) for the high-loss VV case, the direct wave disappears due to the increased loss of the forest layer. The lateral wave still exists in the high loss case as for long ranges most of its path is outside the forest layer. This indeed confirms Tamir's earlier assertion that the lateral wave is the only surviving mechanism in a high-loss forest at large distance.

The above two mechanisms are not sufficient to explain the HH case. In Fig. 4(b), the low-loss HH case, we observe two bands instead of two distinct mechanisms in time. From the time-of-flight analysis, the lateral wave corresponds to the lower edge of the orange band and the direct path corresponds to the lower edge of the red band. The two spreading bands in the HH time profile indicate that there may be multiple propagation paths that cause the time spread. We postulate here that the red band corresponds to multiple reflected waves in the forest slab and the orange band is due to the multi-bounce lateral wave mechanisms. Indeed, such multi-reflected wave and multi-bounce lateral wave mechanisms were suggested earlier by Dence and Tamir [3]. These mechanisms are much more prominent in the HH case because the ground reflection is much stronger for the horizontal polarization than the vertical polarization. The multiple

reflection and multi-bounce lateral waves are illustrated in Figs. 7(a) and 7(b), respectively. Comparing the high-loss case in Fig. 5(b) to the low-loss case in Fig. 4(b), we observe that the multi-reflected waves inside the forest layer die off almost completely at large distances and the multi-bounce lateral waves gets weaker because they spend more time bouncing in the lossy forest.

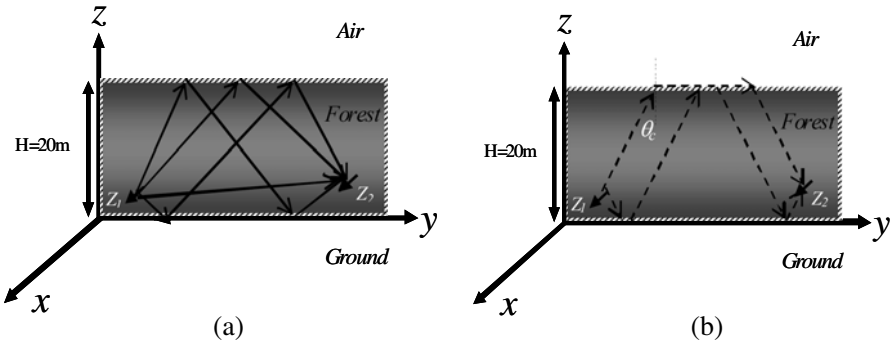

Figure 7. (a) Multi-reflected slab wave. (b) Multi-bounce lateral wave.

To make a more quantitative substantiation of the above observations, we implement the above postulated mechanisms in isotropic forest slab using a ray optical method. First, the ray models for the direct wave and the multi-reflected waves are implemented. As seen from Fig. 7(a), there exist a single direct path and numerous multi-reflected paths between a fixed source and observation point. For each path, the received field can be calculated by:

$$E_{1mn} = j\frac{k\eta P_{x,z}}{4\pi}\frac{e^{-\alpha R_{mn}}e^{-j\beta R_{mn}}(\Gamma_a)^m(\Gamma_g)^n}{R_{mn}} \tag{14}$$

In the above formula, k and η are the wave number and the wave impedance in the forest layer, respectively. P is the source dipole moment as defined before. β and α are the real and imaginary parts of the propagation constant inside the forest, and R_{mn} is the path length. We assume that the ray reflects m times at the forest-air interface and n times at the forest-ground interface. Γ_a and Γ_g denote the reflection coefficients at the forest-air and forest-ground interfaces, respectively. The reflection coefficients for the vertical dipole and horizontal dipoles are different. The contribution of higher order reflections to the total received field decreases as the path length and the number of reflections increase. Therefore, the ray sum converges quickly.

Second, the contributions from the lateral wave and the multi-bounce lateral waves are implemented. Similar to the multi-reflected wave paths inside the forest, there are many multi-bounce lateral wave paths in Fig. 7(b), each of which is expressed as [1]:

$$E_{2mn} = \frac{\eta P_{x,z} e^{-\alpha R_{mnf}} e^{-j\beta R_{mnf}} e^{-jk_o R_{mna}} (\Gamma_a)^m (\Gamma_g)^n}{2\pi R_{mna}^2 R_{mnf} (\varepsilon_{c2} - 1)} \tag{15}$$

The multi-reflected lateral wave path consists of two parts, one is inside the forest and the other is in the air propagating along the forest-air boundary. R_{mnf} and R_{mna} represent the path lengths in the forest layer and in the air layer, respectively. The field along the path inside the forest decays exponentially due to the conductivity of the forest layer, while it decays as r^2 as it propagates along the forest-air boundary.

By combining (14) and (15) for the multi-reflected waves and the multi-bounce lateral waves, the transmission loss versus time delay and range for both the vertical and horizontal polarizations in both a low-loss and a high-loss forest are generated. The results are shown in Fig. 8. Here $m = 10$ and $n = 10$ result in convergent ray sums.

We observe that the transmission loss prediction versus time delay and range given by the ray-optical method agrees quite well with the numerical Sommerfeld results. For the low-loss VV case in Fig. 8(a), the two dominant tracks represent the direct wave and the lateral wave. For the low-loss HH case in Fig. 8(b), the results of the ray optical method indeed support the multi-reflected and multi-bounce lateral wave argument. Both the red band due to the multi-reflected waves and the orange band due to the multi-bounce lateral waves are in good agreement with the numerical Sommerfeld results. In the high-loss cases for both the VV (Fig. 8(c)) and HH (Fig. 8(d)) polarizations, the transmission loss vs. time delay and range given by the ray-optical method is very similar to the Sommerfeld results, with the lateral wave being the dominant mechanism at long distances.

To summarize, the results of the vertical polarization indicate that the direct wave and the lateral wave are the two dominant propagation mechanisms in a low-loss forest. For a high-loss forest, the lateral wave becomes the only surviving mechanism at long distances. The horizontal polarization results are more complex, as multi-reflection and multi-bounce lateral waves have to be included to explain the time-spreading observation.

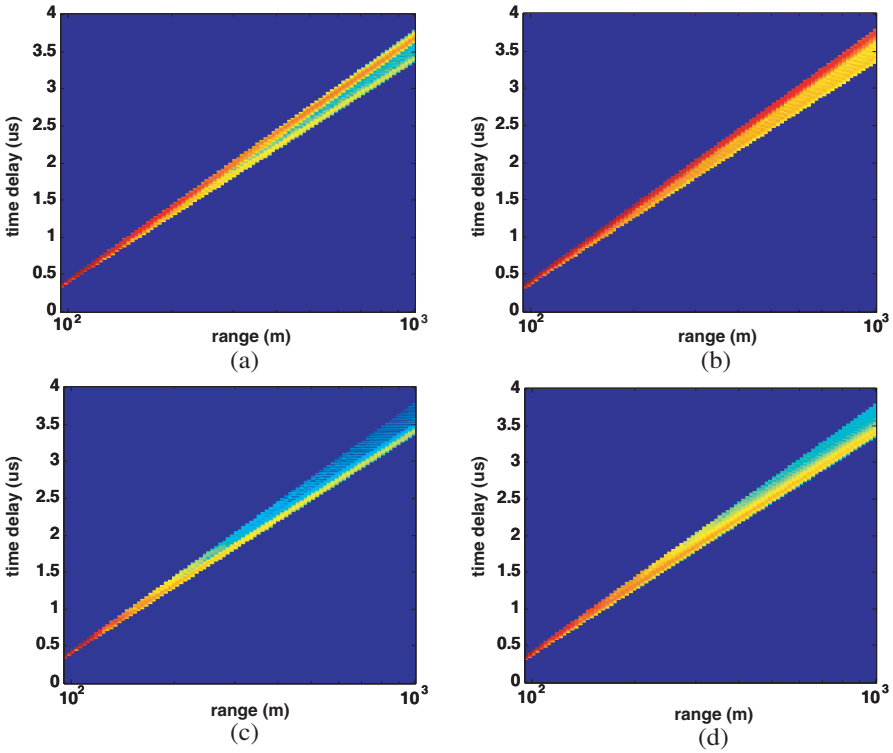

Figure 8. Transmission loss versus time delay and range obtained using ray optics. (a) Low-loss, vertical polarization. (b) Low-loss, horizontal polarization. (c) High-loss, vertical polarization. (d) High-loss, horizontal polarization.

4. EXTRACTION OF EFFECTIVE FOREST PARAMETERS BASED ON THE SLAB MODEL

The studies in the last two sections show that the dominant propagation mechanisms of the slab model depend critically on the effective medium parameters, especially the loss parameters σ_z and σ_t. Therefore, a key question that needs to be addressed is what typical values of these medium parameters should be used so that the slab model can adequately model wave propagation in real forests. In this section, we will use the Sommerfeld solution to extract the forest parameters based on existing measurement data from the literature. In particular, Hicks et al. [16] have collected extensive transmission data in Thailand where there exist areas of large tropical rain forests. One set of their measurement results are used here to illustrate the

extraction procedure.

To obtain an estimation of the forest effective parameters, we use the full anisotropic solution described in Section 2, so that all four parameters, namely, ε_z, ε_t, σ_z and σ_t need to be searched simultaneously to match the measurement results. However, to ease the computation in the inversion process, we carry out the following three steps. First, we obtain the best fit for the HH data only by searching for ε_t and σ_t while keeping ε_z and σ_z at some nominal values. This search can be carried out first since ε_z and the σ_z have essentially no effect on the propagation in the HH case. Second, using the ε_t and σ_t obtained from step one, we search for the best ε_z and σ_z to optimize the VV data fitting. Finally, using the parameters found in steps one and two as the initial guess, we refine these parameters by doing a full four-parameter search using both the VV and HH data. The Matlab local search algorithm *fminsearch* is used to search the optimum parameters in the above three steps. We use other parameters as given by Hicks: the forest effective height is 30.48 m; the relative permittivity and the conductivity of the ground are 15 and 10^{-2} S/m, respectively; the transmitter height is 3.96 m and the distance between the transmitter and the receiver is 1.6 km.

Figures 9(a), (b) and (c) show our fitted data at 25 MHz, 50 MHz and 100 MHz respectively. In Fig. 9, the horizontal axis is the receiver height which changes from 7.01 m to 28.96 m and the vertical axis represents the transmission loss between the transmitter and the receiver. As can be seen from all three figures, our fitted curves agree with the measurement data quite well at all three frequencies. Our fitted parameters are summarized in Table 1. We observe that the relative permittivity in the horizontal direction ε_t is quite stable and close to 1.01 for all three frequencies. ε_z, the relative permittivity in the vertical direction, also has fitted values in this range, but shows a slight frequency dependence. The effective conductivity values σ_z and σ_t both show more significant change as a function of frequency. As expected, σ_z is larger than σ_t at all three frequencies. This can be attributed to the stronger scattering of the vertically polarized electric field due to the vertical tree trunks. The contrast between σ_z and σ_t is strongest at the low frequency end of 25 MHz. As frequency increases, σ_z decreases while σ_t shows the opposite trend. This result implies that as frequency increases, the anisotropy of the equivalent forest slab becomes less pronounced.

It is interesting to note that in Hicks' report the measured transmission loss inside the forest was also fitted to a slab model based on the lateral wave approximation. In their fit, the VV and HH data were fitted separately to an isotropic model. Furthermore, all four

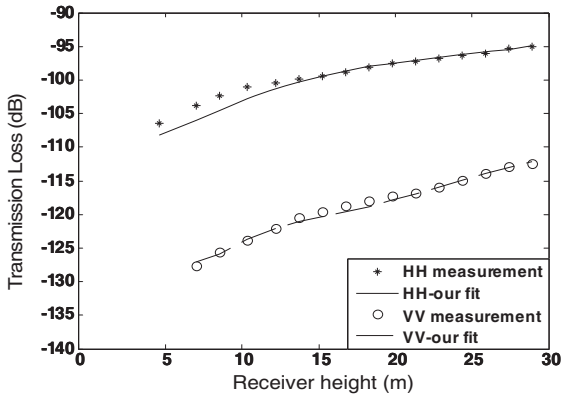

(a) 25MHz

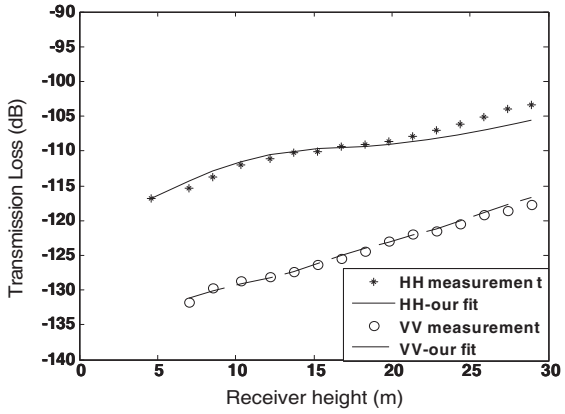

(b) 50MHz

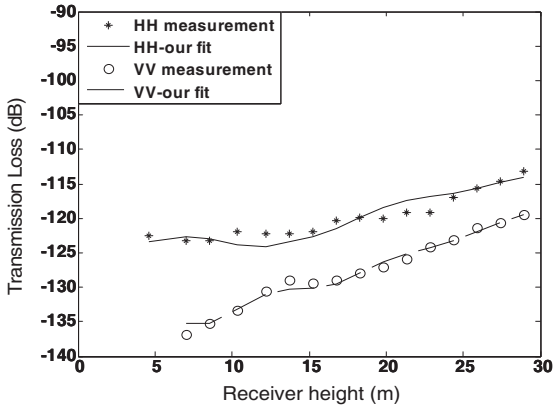

(c) 100MHz

Figure 9. Comparison between the sommerfeld solution with fitted medium parameters and Hicks' measurement data: (a) 25 MHz. (b) 50 MHz. (c) 100 MHz.

Table 1. Fitted medium parameters using Hicks' measurement data based on the Sommerfeld solution.

Freq (MHz)	ε_z	ε_t	σ_z ($\times 10^{-3}$ S/m)	σ_t ($\times 10^{-3}$ S/m)
25	1.053	1.008	0.118	0.030
50	1.018	1.010	0.073	0.037
100	1.006	1.010	0.045	0.042

Table 2. Averaged difference between the Sommerfeld solution and Hicks measurement data.

Averaged difference between the Sommerfeld solution and measurement (dB)	25 MHz		50 MHz		100 MHz	
	VV	HH	VV	HH	VV	HH
Our fitted values	0.3	0.6	0.4	0.8	0.4	0.9
Hicks' fitted values	11.4	5.7	5.9	3.1	6.2	6.6

electrical parameters were assumed to be constant across frequency. Their fitted relative permittivity of the forest was found to be 1.01 for both polarizations and the conductivities were 0.03 mS/m for the horizontal polarization and 0.04 mS/m for the vertical polarization across the frequency band. The averaged fitting errors between the Sommerfeld solution based on our fitted values and the measured data are listed in the first row entry of Table 2. For comparison, we also compute the fitting errors using Hicks' fitted values in the Sommerfeld solution against the measured data. The resulting errors are listed in the second row entry of Table 2. The comparison of the errors clearly show that our fitted values, obtained based on the Sommerfeld solution and done one frequency at a time, lead to a much improved fitting of the measured data.

5. CONCLUSIONS

In this paper, we have implemented the Sommerfeld integral solution to the anisotropic slab model, derived previously by Li et al., to model forest propagation. The solution was used to generate broadband propagation data over range, height, frequency and polarization. The broadband data were then transformed to the time domain to identify the various times-of-flight. Since different propagation paths have different time delays, the propagation mechanisms were well revealed in

this manner. It was found that the direct path, the lateral wave, the multi-reflected slab waves, and the multi-bounce lateral waves could all exist in the forest layer. Based on the most important propagation mechanisms, a ray-based predictor was also implemented to generate an approximate solution and verify the mechanism interpretation.

The propagation mechanisms were found to be strongly dependent on the effective medium parameters of the forest in the slab model. In particular, the anisotropic conductivities of the forest are crucial in determining the dominant propagation mechanism inside the forest layer. Therefore, we applied the Sommerfeld solution to extract the effective forest parameters based on the published measurement data of Hicks et al.. The agreement between the resulting fitted model and measured data was found to be good, and the extracted effective permittivity and conductivity of the forest layer showed interesting anisotropy and frequency dependence.

Further verifications on the forest propagation mechanisms as predicted by the slab model would require more carefully designed experiments in the forest. This could be quite a difficult undertaking. A possible alternative is to use large-scale numerical computation to produce detailed simulation data to facilitate the further understanding of forest propagation. This topic is currently being pursued.

ACKNOWLEDGMENT

This work is supported by the National Science Foundation under grant ECCS-0725729.

REFERENCES

1. Tamir, T., "On radio-wave propagation in forest environments," *IEEE Trans. Antennas Propagat.*, Vol. 15, 806–817, Nov. 1967.
2. Sachs, D. L. and P. J. Wyatt, "A conducting slab model for electromagnetic propagation within a jungle medium," *Radio Sci.*, Vol. 3, 125–134, 1968.
3. Dence, D. and T. Tamir, "Radio loss of lateral waves in forest environments," *Radio Sci.*, Vol. 4, 307–318, Apr. 1969.
4. Tamir, T., "Radio wave propagation along mixed paths in forest environment," *IEEE Trans. Antennas Propagat.*, Vol. 25, 471–477, Jul. 1977.
5. Brown, G. S. and W. J. Curry, "A theory and model for wave propagation through foliage," *Radio Sci.*, Vol. 17, 1027–1036, Sept./Oct. 1982.

6. Cavalcante, G. P. S., D. A. Rogers, and A. J. Giardola, "Analysis of the electromagnetic wave propagation in multilayered media using dyadic green's function," *Radio Sci.*, Vol. 17, 503–508, May/Jun. 1982.
7. Cavalcante, G. P. S. and A. J. Giardola, "Optimization of radio communication in media with three layers," *IEEE Trans. Antennas Propagat.*, Vol. 31, 141–145, Jan. 1983.
8. Matthaeis, P. D. and R. H. Lang, "Microwave scattering models for cylindrical vegetation components," *Progress In Electromagnetics Research*, PIER 40, 131–153, 2003.
9. Huang, E. X. and A. K. Fung, "Electromagnetic wave scattering from vegetation with odd-pinnate compound leaves," *Journal of Electromagnetic Waves and Applications*, Vol. 19, No. 2, 231–244, 2005.
10. Li, L. W., T. S. Yeo, P. S. Kooi, M. S. Leong, and J. H. Koh, "Analysis of electromagnetic wave propagation in forest environment along multiple paths," *Journal of Electromagnetic Waves and Applications*, Vol. 13, 1057–1059, 1999.
11. Sarabandi, K. and I.-S. Koh, "Effect of canopy-air interface roughness on HF-VHF wave propagation in forest," *IEEE Trans. Antennas Propagat.*, Vol. 50, No. 2, 111–121, Feb. 2002.
12. Li, L. W., J. H. Koh, T. S. Yeo, M. S. Leong, and P. S. Kooi, "Cylindrical vector eigenfunction expansion of green dyadics for multilayered anistropic media and its application to four-layered forest," *IEEE Trans. Antennas Propagat.*, Vol. 52, 466–477, Feb. 2004.
13. Whale, H. A., "Radio propagation through New Guinea rain forest," *Radio Sci.*, Vol. 3, 1038, Oct. 1968.
14. Tewari, R. K., S. Swarup, and M. N. Roy, "Radio wave propagation through rain forests of India," *IEEE Trans. Antennas Propagat.*, Vol. 38, 433–449, Apr. 1990.
15. Rogers, R. L. and H. Ling, "Extended line-of-sight communications for unattended ground sensors," Final Report, DARPA Unattended Ground Sensor Program, Dec. 2005.
16. Hicks, J. J., A. P. Murphy, E. L. Patrick, and L. G. Sturgill "Tropical propagation research," Research and Engineering Dept., Atlantic Research Corp., Alexandria, Va., Nov. 1969.
17. Ling, H. and J. Moore, "Scattering by conductor-backed dielectric gaps," Rome Air Development Center Tech. Report, F49620-88-C-0053, Sep. 1990.
18. Hagn, G. H. and H. W. Parker, "Feasibility study of the

use of open-wire transmission lines, capacitors and cavities to measure the electrical properties of vegetation," Stanford Research Institute Tech. Rept. 13, Aug. 1966.

19. Parker, H. W. and W. Makarabhiromya, "Electric constants measured in vegetation and in Earth at five sites in Thailand," Stanford Research Institute Special Tech. Rept. 43, Menlo Park, California, 1967.
20. Pounds, D. J. and A. H. LaGrone, "Considering forest vegetation as an imperfect dielectric slab," Electric Engrg. Research Lab., University of Texas, Austin, Tech. Rept. 6-53, May 1963.
21. "IEEE guide for measurements of electromagnetic properties of Earth media," IEEE Std. 356-2001, IEEE Antennas Propagat. Soc., Jun. 2002.